

**Sintering Mechanisms of High-Performance Garnet-type Solid
Electrolyte Densified by Spark Plasma Sintering**

Hirotooshi Yamada*, Tomoko Ito, Rajendra Hongahally Basappa

Graduate School of Engineering, Nagasaki University

1-14, Bunkyo-machi, Nagasaki, 852-8521 Japan

* To whom correspondence should be addressed.

Dr. Hirotooshi Yamada

Phone/Fax: +81-95-8192861

E-mail: h-yama@nagasaki-u.ac.jp

1-14, Bunkyo-machi, Nagasaki, 852-8521 Japan

Abstract

Garnet-type solid electrolyte $\text{Li}_{6.5}\text{La}_3\text{Zr}_{1.5}\text{Ta}_{0.5}\text{O}_{12}$ (LLZT) was densified by using a spark plasma sintering (SPS) technique. Formation of impurities in the obtained pellets was studied in detail. It is revealed that impurities are strongly related to the SPS process: electrolysis of LLZT and electromigration of graphite. The electrolysis results in $\text{La}_2\text{Zr}_2\text{O}_7$ on anode of the SPS process, which is accompanied by reduction of Li_2CO_3 to amorphous carbon on cathode. The electrolysis on SPS could be successfully suppressed by employing LLZT powder without Li_2CO_3 . When these impurities were removed, pellets obtained by SPS exhibited electrochemical performance comparable with those densified by other methods: total ionic conductivity of $6.9 \times 10^{-4} \text{ S cm}^{-1}$ at 298 K and short-circuit prevention up to $100 \mu\text{A cm}^{-2}$ on dc polarization. The results confirm great advantage of SPS on manufacturing the dense garnet-type solid electrolytes: a low-temperature (900-1100°C) and short-sintering-time process (10 min).

Keywords: Solid electrolyte; Garnet; Spark plasma sintering; Impurity; Short circuit

1. Introduction

All solid-state batteries (ASSBs) have attracted great interests due to their potential application to large-scale energy storage devices [1-3]. Potential advantages of ASSBs are larger energy density, higher safety and higher reliability in comparison with conventional lithium ion batteries. Solid electrolytes are the key materials of ASSBs, and a wide variety of researches have been conducted from development of high ionic conductors [4-12] to interfacial phenomena [1,13-19]. During the last decade, much attention has been paid to a group of lithium ion conductors, originally explored by Weppner's group [6-8]. These solid electrolytes have crystal structure that is similar to that of garnet, and exhibit a general formula $\text{Li}_x\text{B}_y\text{C}_z\text{O}_{12}$ ($B = \text{Ca, Sr, Ba, La}$; $C = \text{Zr, Nb, Ta, etc.}$ [9]). Especially, $\text{Li}_7\text{La}_3\text{Zr}_2\text{O}_{12}$ (LLZ) (with partial substitution of Li by Al and/or Zr by Nb, Ta) has attracted interests due to their relatively high ionic conductivity of $> 10^{-4} \text{ S cm}^{-1}$ at room temperature. In comparison with sulfide-based solid electrolytes (ionic conductivity: $> 10^{-2} \text{ S cm}^{-1}$ at room temperature) [10-12], lithium ionic conductivity of the garnet-type solid electrolytes may be still low for their practical application. However, the garnet-type solid electrolytes wouldn't produce toxic materials on exposure to air, which is an important issue on their application to large-scale energy storage systems. The most attractive feature of garnet-type solid electrolytes is their

superb electrochemical stability, which may realize lithium metal anode to expand energy density of ASSBs.

When lithium metal is used as an anode of ASSBs, it is important to prepare dense solid electrolytes without through-holes. It is reported that short-circuit occurs during galvanostatic lithium deposition even for solid electrolytes with relative density higher than 90% [20-25]. The short-circuit is supposed to be caused by the deposited lithium growing through voids among grains [24]. To obtain well-sintered garnet-type solid electrolytes by conventional sintering processes, generally high temperature ($> 1200^{\circ}\text{C}$) and long sintering time (> 30 h) are required. Even if hot press is employed, high temperature is necessary. Such high-temperature processes (and long duration time) often result in decomposition of solid electrolytes and loss of Li.

Spark plasma sintering (SPS), which is also known as field assisted sintering technique (FAST) or pulsed electric current sintering (PECS), is one of techniques to sinter materials with assistance of uniaxial pressure and pulsed electric current [26-28]. The current through specimens and/or die generates large local joule heat to facilitate sintering of particles. Baek et al. reported fabrication of sintered $\text{Li}_{7-x}\text{La}_3\text{Zr}_{2-x}\text{Ta}_x\text{O}_{12}$ (LLZT) by SPS [26]. They reported ionic conductivity of the obtained LLZT was comparable to specimens prepared by conventional sintering processes in spite of rather

low process temperature (900-1100°C) and very short process time (10 min). Zhang, et al. prepared a highly dense pellet of Al-doped LLZ (relative density: 99.8%) by SPS at 1150°C for 10 min [27]. In these report, impurity ($\text{La}_2\text{Zr}_2\text{O}_7$) was formed after SPS, which increased with increasing process temperature of SPS. The mechanism of the impurity formation is not revealed yet, and further detailed studies are required to see whether SPS is a useful process or not.

In this work, local structure of LLZT pellets prepared by SPS was investigated in detail, especially with respect to the formation of impurity. Further, lithium ionic conductivity and short-circuit prevention were also examined to study the possibility of practical application of SPS-prepared LLZT to ASSBs.

2. Experimental

2.1. Preparation of LLZT Pellets

LLZT powder was synthesized by solid-state reaction using $\text{LiOH}\cdot\text{H}_2\text{O}$ (Kishida Chemical Co. Ltd., 99.0%), La_2O_3 (Kishida Chemical Co. Ltd, 99.99%), ZrO_2 (Kishida Chemical Co. Ltd., 99.9%) and Ta_2O_5 (Wako Pure Chemical Industries Ltd., 99.9%). $\text{LiOH}\cdot\text{H}_2\text{O}$ and La_2O_3 were heated at 200°C and 800°C, respectively, in advance to remove water and CO_2 . Excess LiOH was added by 10% to compensate loss of Li by

volatilization during the following calcination. The starting powder was mixed using a planetary ball-mill using ZrO₂ balls (ϕ 3 mm) and a ZrO₂ pot with a rotation rate of 300 rpm for 1 hour. Then, the mixed powder was calcined in aluminum crucible for 900°C for 12 hours. At this calcination temperature, Al contamination from the crucible was not confirmed. SPS was conducted on a CSP-I-02121 (SS Alloy Co Ltd.) using graphite die and punches (diameter 10 mm). Graphite sheets were inserted between powder and the graphite mold for facile demolding after SPS.

SPS was carried out under vacuum (initial chamber pressure was below 10 Pa), dc pulse current was applied to control the temperature, which was monitored on outer surface of the graphite die using a thermo-couple. Specimens were heated with a ramp rate of 50°C/min toward a target temperature (900-1100°C), and held at the target temperature for 10 min. Then, the samples were cooled inside the chamber. During the sintering, a constant uniaxial pressure (12.5-50 MPa) was applied. The obtained pellets were typically 10 mm in diameter and 1 mm in thickness (after the graphite sheets were removed).

As the garnet-type solid electrolytes are sensitive to moisture and CO₂ [29,30], the LLZT powder and pellets were stored in vacuum-desiccators to minimize the formation of surface impurities. Typical exposure time to air was less than 1 hour. To investigate the

influence of H₂O and CO₂ (resulting in Li₂CO₃ on the surface of LLZT particles) on SPS, Li₂CO₃-free LLZT powder and pellets were prepared by modifying the preparation process as follows. First, LiOH·H₂O, ZrO₂ and Ta₂O₅ were vacuum-dried at 200°C in a glass-tube oven, which was directly transferred into an Ar-filled glovebox. La₂O₃ was pre-heated at 800°C in dry oxygen gas using a furnace connected to the glovebox. Next, the starting materials were mixed in the glovebox, and then, the powder was calcined at 900°C for 12 h in dry oxygen gas using the furnace connected to the glovebox. Then, the calcined LLZT powder was put into a graphite die and sealed in the glovebox, and transferred into the SPS chamber. Finally, after SPS, the pellets were taken out of the die and stored in the glovebox.

2.2. Characterization

Crystalline structures of calcined and sintered LLZT were investigated by X-ray diffraction (XRD) on SmartLab (Rigaku Corp., CuK α , 45 kV, 200 mA) equipped with a parallelized incident beam. Soller slits (5°) for both incident and diffracted beams and a parallel slit analyzer (0.5°) were used. An incident slit and two receiver slits were 1.0 mm and 0.4 mm in width, respectively. A graphite monochromator was placed in front of a scintillation counter to suppress fluorescent X-ray. Diffraction was recorded every 0.02°

step by $2\theta/\theta$ scan with a scan rate of $2.0^\circ/\text{min}$. For detailed structural analysis, step-scan was employed with an accumulation time of 10 sec at each angle. The structure refinement was conducted by Rietveld method using RIETAN-FP [31].

Density of pellets was obtained using the dimensions and weight of pellets. The relative density was calculated by comparing the geometric density with the density estimated from lattice constant (5.36 g cm^{-3}).

Morphology of surface and fractural cross-section of sintered pellets were observed by field-emission scanning electron microscope (FE-SEM) on a JSM-7500F (JEOL Ltd.). Distribution of elements was confirmed by energy dispersive spectroscopy (EDS) attached on FE-SEM.

2.3. Electrochemical Measurements

Electrochemical impedance spectroscopy (EIS) was conducted to obtain ionic conductivity of sintered pellets. The EIS was recorded in the frequency range from 1 MHz to 0.1 Hz with an oscillation voltage of 10 mV using a frequency response analyzer (S1260, Solartron Analytical). Before EIS measurements, surface of sintered pellets were polished using an emery paper (#1500) to remove surface impurities, and gold electrodes with a thickness of ca. 300 nm were deposited on both sides by dc sputtering. Then, the

pellets were set in a homemade two-electrode cell in which Ar gas flowed. The cell was heated up to 110°C and cooled down to 15°C with a very slow ramp rate of 0.25°C/min to achieve quasi-equilibrated state. The EIS was repeatedly recorded every 10 min on the heating and the cooling processes. The temperature of the specimens was monitored by a thermo-couple that was placed near the pellet. Dc polarization was conducted for a symmetric cell of Li | LLZT | Li to obtain the critical current density at which short-circuit occurs. The symmetric cell was assembled in an Ar-filled glovebox as follows: first, surface of a Li foil was scraped using a stainless steel spatula, then the foil was cut into disks (5 mm and 1.5 mm in diameter and thickness, respectively), which were embedded in the Al₂O₃ washer (with outer and diameter of 10 mm and 5 mm, respectively) to avoid deformation of lithium disks by pressure and heat. Next, the Li electrodes were attached on both sides of LLZT that was polished in advance using emery paper (grit number #4000) to remove surface impurity. Finally, the obtained Li | LLZT | Li was placed in a gas-tight stainless steel cell, in which uniaxial pressure of 1.4 MPa was applied by a spring. To improve the contact between Li and LLZT, the cell was heated at 180°C for 3 hours. During heating, EIS was conducted to see the change in the interfacial resistance as well as to improve the contact by the repetitive Li deposition and dissolution on the both electrodes. Dc polarization was conducted with current densities of 20, 50, 100, and 200

$\mu\text{A cm}^{-2}$ at 25°C . The current was applied in one direction for 30 min and then the direction was switched. The current cycle was repeated for 5 cycles at each current density.

3. Results and Discussion

3.1. Structure of LLZT Pellets

Figure 1 shows XRD profiles of LLZT powder before and after the SPS operated at 900°C and 50 MPa for 10 min. The LLZT powder after the SPS (Figure 1(a), top) was obtained by grinding a sintered pellet using an agate mortar. Before the SPS (Figure 1(a), middle), all of the diffraction peaks could be indexed with a space group of $Ia\bar{3}d$ (No. 230) and a lattice parameter of $a = 12.9497(2) \text{ \AA}$, which is comparable to reported values ($a = 12.9307(4)$ [32], $12.94099(7) \text{ \AA}$ [33], 12.958 \AA [34]). After the SPS, $\text{La}_2\text{Zr}_2\text{O}_7$, Li_2CO_3 and graphite were confirmed as impurities. After the SPS, diffraction peaks attributed to the garnet-phase shifted towards lower angle and asymmetrically broadened (Figure 1(b) middle). Furthermore, position and shape of peaks returned toward those of original powder after ground (Figure 1(b), top). Botros et al. explained that the shift and broadening is due to the formation of a distorted garnet phase [28]. The Rietveld refinement of the XRD profile of a LLZT pellet (Figure S1, Supplementary Information S1) converged with poor fitting. The refinement indices may not be satisfactory ($R_{\text{wp}} =$

7.47%, $R_{wp}/R_e = 2.50$), which suggests insufficient structural model. For example, distribution of lattice parameters as well as local deviation of composition may be induced by the SPS. However, it is beyond the scope of this work to determine the crystalline structure in detail, and further investigation is required. As for the impurities, the graphite is likely originated from the graphite sheets inserted between the specimen and the punches, while Li_2CO_3 and $\text{La}_2\text{Zr}_2\text{O}_7$ resulted from the decomposition of LLZT. The details on the impurity formation will be investigated later.

Figure 2 shows SEM images of LLZT sintered by SPS (with a relative density of 96%). On the polished surface (Figure 2(a)), although the pellet seems rather dense, a few cracks were confirmed, which may allow dendritic growth of Li and short-circuit through the pellet. In fractured cross-section images (Figure 2(b, c)), the densely packed grains are confirmed. It should be noted that while shape of grains is not obvious in the secondary electron image (Figure 2(b)), grains were clearly observed in the reflection electron image (Figure 2(c)), which indicates certain phase(s) consisting of light elements are accumulated on grain boundaries. Li_2CO_3 is the most plausible candidate for such a phase. On the surface of LLZT particles, thin Li_2CO_3 layer is formed by reaction with H_2O and CO_2 on exposure to air [29,35]. The Li_2CO_3 layer on the LLZT particle was also suggested by Raman spectra (Figure S2) and TEM images (Figure S3). Although FE-

SEM-EDS was taken to reveal distribution of Li_2CO_3 , it was difficult to obtain clear evidence of carbon accumulation on the grain boundaries. This would be partly because the energy of X-ray of C $\text{K}\alpha$ and O $\text{K}\alpha$ is close (0.28 keV and 0.52 keV for C and O, respectively), resulting in inaccuracy in quantitative analysis. In Figure 2(c), there are several dark spots among grains, in addition to the dark thin layer on grain-boundary (as denoted above). These spots are supposed to be Li_2CO_3 accumulated above its melting point (720°C).

In comparison with the round particles of original LLZT powder (Figure S4(a)), grains in the LLZT pellet seems rather flat without change in the average grain size (Figure S4(b)). This resulted from the pressure on the SPS (applied in the horizontal direction of Figure S4(b)). The deformed grains suggest that LLZT particles were sintered not by surface diffusion as in conventional high temperature sintering, but by plastic deformation on the SPS, which might have also caused distortion of crystal lattice.

3.2. Impurities in LLZT Pellets

Figure 3 shows optical images of a pellet obtained by the SPS. In the fractured cross-section image (Figure 3(a)), it is clear that a region near the bottom looked black. The bottom of the pellet corresponds to the cathode of the dc pulse of the SPS. The black

stain was confirmed even after the cathode side of the pellet was polished by 150 μm (Figure 3(c, d)), while no stain was confirmed on the anode (Figure 3(b)). The asymmetric coloration suggests inhomogeneous distribution of impurity phases, and XRD was conducted to investigate the impurity distribution. First, the graphite sheets were removed using emery paper (grit number #400). Then, the surface of the pellets was polished by certain thickness (typically 50-100 μm), which was followed by XRD measurement. This process was repeated until impurities disappeared. Note that the attenuation length of X-ray (wavelength: 0.154 nm) in LLZT ranges from 1 to 6 μm in the experimental condition (2θ : 20 to 90°) (Figure S5, Supplementary Information S4). Therefore, XRD shows phases on surface of pellets after polished. Figure 4(a) shows, $\text{La}_2\text{Zr}_2\text{O}_7$ were confirmed up to 150 μm from the surface of the anode. On the other hand, on the cathode, only trace of Li_2CO_3 was detected and no reduced products originated from LLZT such as Zr_3O [36] were confirmed even by XPS (Figure S7, Supplementary Information S5).

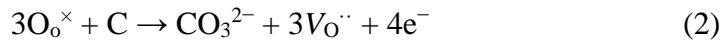
Interestingly, the formation of $\text{La}_2\text{Zr}_2\text{O}_7$ was dependent on particle size of LLZT powder used for the SPS. When as-calcined LLZT powder (1-2 μm in diameter) was used, $\text{La}_2\text{Zr}_2\text{O}_7$ distributed for ca. 200-300 μm from the surface of the anode (Figure 4(a)). However, for ball-milled powder (~200 nm in particle size), $\text{La}_2\text{Zr}_2\text{O}_7$ exhibited strong

diffraction peaks even after surface layer was removed by 1 mm by polishing (Figure 4(b)).

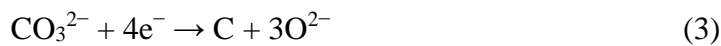
Taking account of the above results, the formation of $\text{La}_2\text{Zr}_2\text{O}_7$ is explained by release of oxygen from the lattice due to the oxidation on the anode, which is shown in the following equations (in Kröger-Vink notation) [37,38]:



and/or



In Eq. (1), oxygen ions in the garnet lattice are oxidized, resulting in oxygen gas evolution, while graphite is oxidized to form carbonate ions in Eq. (2). Even when gold thin foils were used instead of the graphite sheets to avoid Eq. (2), $\text{La}_2\text{Zr}_2\text{O}_7$ was still confirmed on the anode (data are not shown). Therefore, the decomposition of LLZT is mainly caused by Eq. (1). Note that electrochemical oxidation on the anode should be accompanied with reduction on the cathode. Nevertheless, reduced impurities were not detected by XRD and XPS, although it was obviously blackened. The black impurity is possibly amorphous carbon produced by the reduction of Li_2CO_3 existing on LLZT particles [37]:



Oxygen ions (O^{2-}) would be paired with Li^+ to produce Li_2O , which may be further turned into $LiOH$ or Li_2CO_3 after exposed to air. Or O^{2-} may diffuse towards the anode.

To confirm the influence of Li_2CO_3 , pellets were fabricated by SPS using LLZT powder that was synthesized in an atmosphere without H_2O and CO_2 (dry Ar, O_2 or vacuum). Li_2CO_3 -free LLZT powder thus obtained exhibited no impurities and the same lattice parameter: $a = 12.950(7) \text{ \AA}$. In addition, Li_2CO_3 -free LLZT pellet contained neither $La_2Zr_2O_7$ nor amorphous carbon.

These results can be reasonably explained by electrode potential. The electrode potential for CO_3^{2-} reduction to amorphous carbon (Eq. (3)) is $E(C/CO_3^{2-}) = 1.1 \text{ V vs. Li/Li}^+$ (450°C) [37]. Other possible reductions would be the reduction of LLZT [36] and Li deposition, i.e.,



As the reduction potential of Eq. (3) is the highest, the electrolysis voltage of the electrolysis pair of Eqs. (1) and (3) ($V(1-3)$) are lower than those of Eqs. (1) and (4) ($V(1-4)$), and Eqs. (1) and (5) ($V(1-5)$). Taking account of the experimental results, it is supposed that the applied voltage during the SPS ($V(\text{SPS})$, 4~4.5 V) is between these values as follows:

$$V(1-3) < V(\text{SPS}) < V(1-4), V(1-5). \quad (6)$$

This order indicates the possible electrolysis pair is only Eqs. (1)-(3), which proceeds only on the presence of Li_2CO_3 . In other words, without Li_2CO_3 , no electrolysis occurs. On the other hand, when more Li_2CO_3 is included, more electrolysis proceeds. This is why more $\text{La}_2\text{Zr}_2\text{O}_7$ was produced when milled LLZT powder was used (Figure 4(b)).

Although electrolysis could be successfully avoided by excluding Li_2CO_3 from LLZT powder, graphite intrusion was still confirmed on the cathode. To understand this phenomenon, a LLZT pellet was prepared by using Au thin foils instead of graphite sheet to prevent direct contact of LLZT with graphite. Figure 6(b) shows reflection electron images of the cross-section of the pellet, in which bright spots with a diameter of ca. 1 μm were distributed in the pellet especially on the cathode. By comparing a reflection electron image (Figure S8(a)) with EDS mapping images (Figure S8(b)-(f)), it is confirmed that the bright spots were Au (note that homogeneous background signal of Au is due to Au thin layer deposited to avoid charging-up on electron beam). Therefore, it was revealed that SPS causes fragmentation of the gold thin foil on the cathode. The fragmentation of thin foils and intrusion into the cathode can be well explained by electromigration, which is often reported for narrow wires in large-scale integration (LSI) [39]. The electron flux on the large current density ($\sim 500 \text{ A cm}^{-2}$) scatters atoms on their

conduction path with their huge momentum, which leads fragmentation and intrusion of the foils. In this experiment, Au foil was just employed for the demonstration of the electromigration, however, when graphite foils are used as usual, fragmentation and intrusion of graphite occurs. To avoid the electromigration, metals with high melting point may be effective because of their high lattice energy. However, as far as we tried, Ti foils (melting point: 1668°C) also exhibited electromigration.

3.3. Electrochemical Properties

Ionic conductivity of the LLZT pellets was obtained by electrochemical impedance after impurities ($\text{La}_2\text{Zr}_2\text{O}_7$, graphite and amorphous carbon) were removed by polishing the surface of the pellets using emery paper (grit number #400). Figure S9 shows Nyquist plots recorded at 25°C for two symmetric cells Au | LLZT | Au (ion blocking electrodes) and Li | LLZT | Li (reversible electrodes) using a same LLZT pellet. For Li | LLZT | Li, the Nyquist plot consists of two parts: a tail of a semi-circle for the frequencies higher than 10^5 Hz and a depressed semicircle in the frequency range from 10^4 to 10 Hz. On the other hand, Au | LLZT | Au exhibited a tail of a semi-circle ($> 10^5$ Hz) and a sloped straight line. By comparing the frequency ranges and characteristic frequency of obtained results and reported values, the high frequency part observed for both electrode systems is

ascribed to a part of grain-boundary resistance [32,40], while a large semi-circle for the Li electrodes is charge transfer resistance (R_{ct}) between Li and LLZT [24,25,41]. Small difference in the impedance in the high frequency range is derived from the different thickness of the LLZT pellet, because the same LLZT pellet were polished to remove Au electrodes before Li electrodes were attached. Compared with other reports, R_{ct} (1.3 k Ω cm² for one side) was rather large in this work, just because the preparation of Li electrodes was not optimized yet. The optimization of the R_{ct} will be reported elsewhere.

The Nyquist plot of the Au electrode seems slightly curved around 10³ Hz, which can be found in many reports on garnet-type solid electrolytes [24,25,32]. Although this electrochemical process is not fully explained yet, this is probably due to the surface resistive layer formed during the exposure to air before deposition of Au electrodes after polishing [30,32]. Therefore, total conductivity of LLZT pellets was obtained from the intercept on the real axis of the extrapolated straight (or curved line) around 10⁴ Hz. Figure S10 demonstrates the temperature dependence of total conductivity (σ) during a cycle of heating to 130°C, holding and cooling to 15°C with a ramp rate of 0.25°C/min. The difference of data recorded on heating and cooling were less than 6%, suggesting the measurements were conducted in the quasi-equilibrated state. The temperature dependence of σ seems to consist of two slopes: the slope in high temperature range is

smaller than those in low temperature range. This can be explained by the change in the contribution of bulk and grain-boundary resistance [42], according to the following analysis: Figure 7(a) shows a Nyquist plot of a thick LLZT pellet (3.3 mm) recorded at 16°C, in which a semi-circle at the high frequency range is almost converged to the real axis. The plot was fitted by using an equivalent circuit shown in Figure 7(b). A constant phase element for bulk resistance was not used for the calculation because the characteristic frequency is much higher than the upper frequency limit in this study. The specific capacitance of the semicircle was ca. 10^{-9} F, suggesting the semi-circle is attributed to the grain-boundary [28]. Figure 7(c) compares the temperature dependence of the conductivity of each component. Grain-boundary resistance is smaller than bulk in this temperature range and the total conductivity is dominated by bulk resistance. What is more, the activation energy of the grain-boundary resistance (0.453 eV) is larger than bulk (0.364 eV). Therefore, the contribution of grain boundaries to the total conductivity is negligible at high temperature. On the other hand, influence of grain-boundary resistance is increased with decreasing temperature, and the activation energy is increased.

Table S1 compares LLZT pellets prepared by various sintering techniques. LLZT pellets sintered by SPS exhibited comparable performance with those prepared by other techniques, although the process temperature is relatively low and the duration time is

much shorter than other processes. Figure 8 shows temperature dependence of ionic conductivity of the LLZT pellets prepared at 1000°C with different pressures on the SPS. Table 1 summarizes the total ionic conductivity and activation energy sintered with different pressure. Although total conductivity at 298 K was less dependent on the SPS pressure, relative density was increased with the pressure. Further, the activation energy at high temperature range (dominated by bulk resistance) was almost the same for all the specimens, while below 50°C, activation energy decreased with increasing the SPS pressure. These results can be well explained by the fact that the influence of the grain-boundary resistance increases at low temperature range: with increasing the relative density, the grain-boundary resistance is reduced and the contribution of the grain-boundary on the total conductivity is also reduced. These results suggest that if the influence of the grain-boundary could be further reduced, it would increase the total conductivity. For example, using larger LLZT particles is one of the possible ways, because grains don't grow under typical SPS conditions as shown in Figure S4.

Another important factor of the garnet-type solid electrolytes is short-circuit prevention. To investigate the critical current density on short-circuit, gradually increasing current density was applied to a symmetric cell of Li | LLZT | Li using a LLZT pellet with a thickness of 1.81 mm (Figure S11). Cell voltage was rather stable up to ± 100

$\mu\text{A cm}^{-2}$. However, at $\pm 200 \mu\text{A cm}^{-2}$, the voltage dropped suddenly after large fluctuation. It should be noted that above $100 \mu\text{A cm}^{-2}$, voltage increases gradually on one direction, while the voltage was recovered on the opposite current. The voltage increase is caused by loss of contact due to void formation between Li and LLZT on one direction, and recovery of the contact on the other direction by burying the voids [43,44]. The loss of the contact increases local current density, which would accelerate the dendrite formation. The degree of void formation on the Li electrode strongly depends on electrode preparation and microstructure of the surface of solid electrolytes [21]. Although the contact between Li and LLZT is not optimized and R_{ct} was large in this work (Figure S9), the critical current density of $200 \mu\text{A cm}^{-2}$ at room temperature is higher than garnet-type solid electrolytes sintered by other methods as compared in Table 2. The optimization of the electrode interface and its influence on the short-circuit will be reported elsewhere.

4. Conclusion

In this study, sintering process on SPS of garnet-type solid electrolytes LLZT was studied by focusing on impurities. The mechanisms of the impurity formation are strongly related to the features of SPS: electrolysis and electromigration. The electrolysis of LLZT depended on the amount of Li_2CO_3 existing on surface of LLZT particles. By using

Li₂CO₃-free LLZT powder, the electrochemical decomposition could be successfully suppressed. The other mechanism, electromigration, causes intrusion of the cathode materials into the solid electrolyte.

When these impurities were removed, the obtained pellets exhibited electrochemical performance that are comparable with those prepared by other sintering techniques: ionic conductivity $6.9 \times 10^{-4} \text{ S cm}^{-1}$ at 298 K and critical current density of $200 \mu\text{A cm}^{-2}$ for short-circuit. The advantage of SPS was clearly demonstrated: dense solid electrolytes with good performances are available at rather low temperature for short process time. Although LLZT was employed in this work, there are various garnet-type solid electrolytes [45]. Some of them exhibit attractive features like tolerance to moisture [46], but not all specimens were well densified. Therefore, it would be meaningful to sinter other garnet-type solid electrolytes by SPS for further development of ASSBs.

Acknowledgements

Thanks are due to Mr. Hiroshi Furukawa for his technical support on FE-SEM-EDS and XPS. A part of this work was financially supported by a research project, “Advanced Low Carbon Technology Research and Development Program of Japan Science and

Technology Agency for Specially Promoted Research for Innovative Next Generation Batteries (JST-ALCA SPRING)”, which is gratefully acknowledged.

References

- [1] N. Ohta, K. Takada, L. Zhang, R. Ma, M. Osada, T. Sasaki, *Adv. Mater.* 18 (2006) 2226–2229.
- [2] T. Kobayashi, Y. Imade, D. Shishihara, K. Homma, M. Nagao, R. Watanabe, T. Yokoi, A. Yamada, R. Kanno, T. Tatsumi, *J. Power, Sources* 182 (2008) 621–625.
- [3] M. Kotobuki, H. Munakata, K. Kanamura, Y. Sato, T. Yoshida, *J. Electrochem. Soc.* 157 (2010) A1076–A1079.
- [4] Y. Inaguma, L. Chen, M. Itoh, T. Nakamura, T. Uchida, H. Ikuta, M. Wakihara, *Solid State Commun.* 86 (1993) 689-693.
- [5] H. Aono, E. Sugimoto, Y. Sadaoka, N. Imanaka, G. Adachi, *J. Electrochem. Soc.* 136 (1989) 590-591.
- [6] V. Thangadurai, W. Weppner, *Adv. Funct. Mater.* 15 (2005) 107-112.
- [7] R. Murugan, V. Thangadurai, W. Weppner, *Angew. Chem. Int. Ed.* 46 (2007) 7778-7781.

- [8] C. A. Geiger, E. Alekseev, B. Lazic, M. Fisch, T. Armbruster, R. Langner, M. Fechtelkord, N. Kim, T. Pettke, W. Weppner, *Inorg. Chem.* 50 (2011) 1089-1097.
- [9] R. Murugan, V. Thangadurai, W. Weppner, *J. Electrochem. Soc.* 155 (2008) A90-A101.
- [10] Y. Kato, S. Hori, T. Saito, K. Suzuki, M. Hirayama, A. Mitsui, M. Yonemura, H. Iba, R. Kanno, *Nature Energy* 1 (2016) 16030.
- [11] N. Kamaya, K. Homma, Y. Yamakawa, M. Hirayama, R. Kanno, M. Yonemura, T. Kamiyama, Y. Kato, S. Hama, K. Kawamoto, A. Mitsui, *Nature Mater.* 10 (2011) 682-686.
- [12] M. Tatsumisago, A. Hayashi, *Solid State Ionics* 225 (2012) 342-345.
- [13] J. Maier, *Prog. Solid State Chem.* 23 (1995) 171-263.
- [14] H. Yamada, A. J. Bhattacharyya, J. Maier, *Adv. Funct. Mater.* 16 (2006) 525-530.
- [15] H. Yamada, Y. Oga, I. Saruwatari, I. Moriguchi, *J. Electrochem. Soc.* 159 (2012) A380-A385.
- [16] H. Yamada, D. Tsunoe, S. Shiraishi, G. Isomichi, *J. Phys. Chem. C* 119 (2015) 5412-5419.
- [17] T. Okumura, T. Nakatsutsumi, T. Ina, Y. Oriyasa, H. Arai, T. Fukutsuka, Y. Iriyama, T. Uruga, H. Tanida, Y. Uchimoto, Z. Ogumi, *J. Mater. Chem.* 21 (2011) 10051-10060.

- [18] K. Yamamoto, Y. Iriyama, T. Asaka, T. Hirayama, H. Fujita, C.A.J. Fisher, K. Nonaka, Y. Sugita, Z. Ogumi, *Angew. Chem. Int. Ed.* 49 (2010) 4414-4417.
- [19] A. Sakuda, A. Hayashi, M. Tatsumisago, *Chem. Mater.* 22 (2010) 949-956.
- [20] R. Sudo, Y. Nakata, K. Ishiguro, M. Matsui, A. Hirano, Y. Takeda, O. Yamamoto, N. Imanishi, *Solid State Ionics* 262 (2014) 151-154.
- [21] L. Cheng, W. Chen, M. Kunz, K. Persson, N. Tamura, G. Chen, M. Doeff, *ACS Appl. Mater. Interfaces* 7 (2015) 2073-2081.
- [22] Y. Ren, Y. Shen, Y. Lin, C.-W. Nan, *Electrochem. Commun.* 57 (2015) 27-30.
- [23] Y. Suzuki, K. Kami, K. Watanabe, A. Watanabe, N. Saito, T. Ohnishi, K. Takada, R. Sudo, N. Imanishi, *Solid State Ionics*, 278 (2015) 172-176.
- [24] C.-L. Tsai, V. Roddatis, C. V. Chandran, Q. Ma, S. Uhlenbruck, M. Bram, P. Heitjans, O. Guillon, *ACS Appl. Mater. Interfaces* 8 (2016) 10617-10626.
- [25] A. Sharafi, H. M. Meyer, J. Nanda, J. Wolfenstine, J. Sakamoto, *J. Power Sources* 302 (2016) 135-139.
- [26] S.-W. Baek, J.-M. Lee, T. Y. Kim, M.-S. Song, Y. Park, *J. Power Sources* 249 (2014) 197-206.
- [27] Y. Zhang, F. Chena, R. Tu, Q. Shen, L. Zhang, *J. Power Sources* 268 (2014) 960-964.

- [28] M. Botros, R. Djenadic, O. Clemens, M. Möller, H. Hahn, J. Power Sources 309 (2016) 108-115.
- [29] Y. Wang, W. Lai, J. Power Sources 275 (2015) 612-620.
- [30] L. Cheng, E. J. Crumlin, W. Chen, R. Qiao, H. Hou, S. F. Lux, V. Zorba, R. Russo, R. Kostecki, Z. Liu, K. Persson, W. Yang, J. Cabana, T. Richardson, G. Chen, M. Doeff, Phys. Chem. Chem. Phys. 16 (2014) 18294-18300.
- [31] F. Izumi, K. Momma, Solid State Phenom. 130 (2007) 15-20.
- [32] T. Thompson, A. Sharafi, M. D. Johannes, A. Huq, J. L. Allen, J. Wolfenstine, J. Sakamoto, Adv. Energy Mater. 5 (2015) 1500096.
- [33] A. Logéat, T. Köhler, U. Eisele, B. Stiaszny, A. Harzer, M. Tovar, A. Senyshyn, H. Ehrenberg, B. Kozinsky, Solid State Ionics 206 (2012) 33-38.
- [34] H. Buschmann, S. Berendts, B. Mogwitz, J. Janek, J. Power Sources 206 (2012) 236-244.
- [35] L. Cheng, E. J. Crumlin, W. Chen, R. Qiao, H. Hou, S. F. Lux, a V. Zorba, R. Russo, R. Kostecki, Z. Liu, K. Persson, W. Yang, J. Cabana, T. Richardson, G. Chen, M. Doeff, Phys. Chem. Chem. Phys. 16 (2014) 18294-18300.
- [36] F. Han, Y. Zhu, X. He, Y. Mo, C. Wang, Adv. Energy Mater. 6 (2016) 1501590.
- [37] H. Kawamura, Y. Ito, J. Appl. Electrochem. 30 (2000) 571-574.

- [38] Y. Ito, *Tanso*, 248 (2011) 144-151.
- [39] S. M. Spitzer, S. Schwartz, *J. Electrochem. Soc.* 116 (1969) 1368-1372.
- [40] I. N. David, T. Thompson, J. Wolfenstine, J. L. Allen, J. Sakamoto, *J. Am. Ceram. Soc.* 98 (2015) 1209-1214.
- [41] L. Cheng, W. Chen, M. Kunz, K. Persson, N. Tamura, G. Chen, M. Doeff, *ACS Appl. Mater. Interfaces* 7 (2015) 2073-2081.
- [42] W. E. Tenhaeff, E. Rangasamy, Y. Wang, A. P. Sokolov, J. Wolfenstine, J. Sakamoto, N. J. Dudney, *ChemElectroChem* 1 (2014) 375-378.
- [43] S. Majoni, J. Janek, *Solid State Ionics* 85 (1996) 247-250.
- [44] J. Janek, *Solid State Ionics* 131 (2000) 129-142.
- [45] V. Thangadurai, S. Narayanan, D. Pinzar, *Chem. Soc. Rev.* 43 (2014) 4714-4727.
- [46] L. Truong, J. Colter, V. Thangadurai, *Solid State Ionics* 248 (2013) 1-7.

Table 1 Density, conductivity and activation energy of LLZT pellets prepared by SPS at 1000°C for 10 min. The surface of pellets was polished to remove impurities.

| SPS Pressure | Relative density | Total conductivity at 298 K | Activation energy | |
|-----------------|------------------|--|-------------------|---------|
| | | | > 90°C | < 50°C |
| 12.5 MPa | 91.3% | $6.2 \times 10^{-4} \text{ S cm}^{-1}$ | 0.34 eV | 0.48 eV |
| 25.0 MPa | 95.0% | $5.8 \times 10^{-4} \text{ S cm}^{-1}$ | 0.36 eV | 0.46 eV |
| 37.5 MPa | 95.5% | $6.9 \times 10^{-4} \text{ S cm}^{-1}$ | 0.35 eV | 0.42 eV |

Table 2 Critical current density of garnet-type solid electrolytes.

| Sintering method | Material | Relative density | Critical current density | Reference |
|------------------------|---------------------------|------------------|----------------------------------|-----------|
| conventional sintering | Al-doped LLZO | 92% | 134 $\mu\text{A cm}^{-2}$ | [9] |
| conventional sintering | LLZT with Au buffer layer | 92.7% | 150 $\mu\text{A cm}^{-2}$ (25°C) | [24] |
| hot press | Al-doped LLZO | 97±1% | 50 $\mu\text{A cm}^{-2}$ (30°C) | [25] |
| SPS | LLZT | 96% | 200 $\mu\text{A cm}^{-2}$ (25°C) | this work |

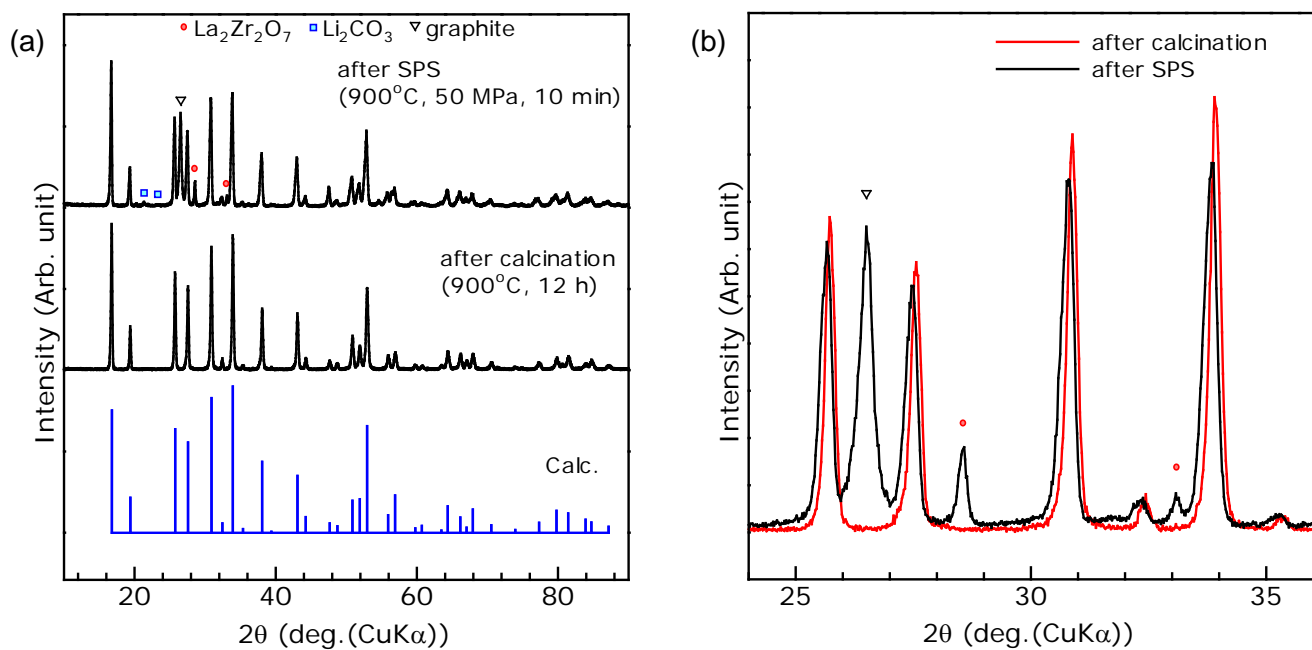


Figure 1. XRD profiles of $\text{Li}_{6.5}\text{La}_3\text{Zr}_{1.5}\text{Ta}_{0.5}\text{O}_{12}$ prepared in this study. (a) (Top) A pellet sintered by SPS at 900°C for 10 min under 50 MPa., (middle) powder after calcination, and (bottom) a calculated profile for comparison. (b) Expanded profiles of after calcination and after SPS.

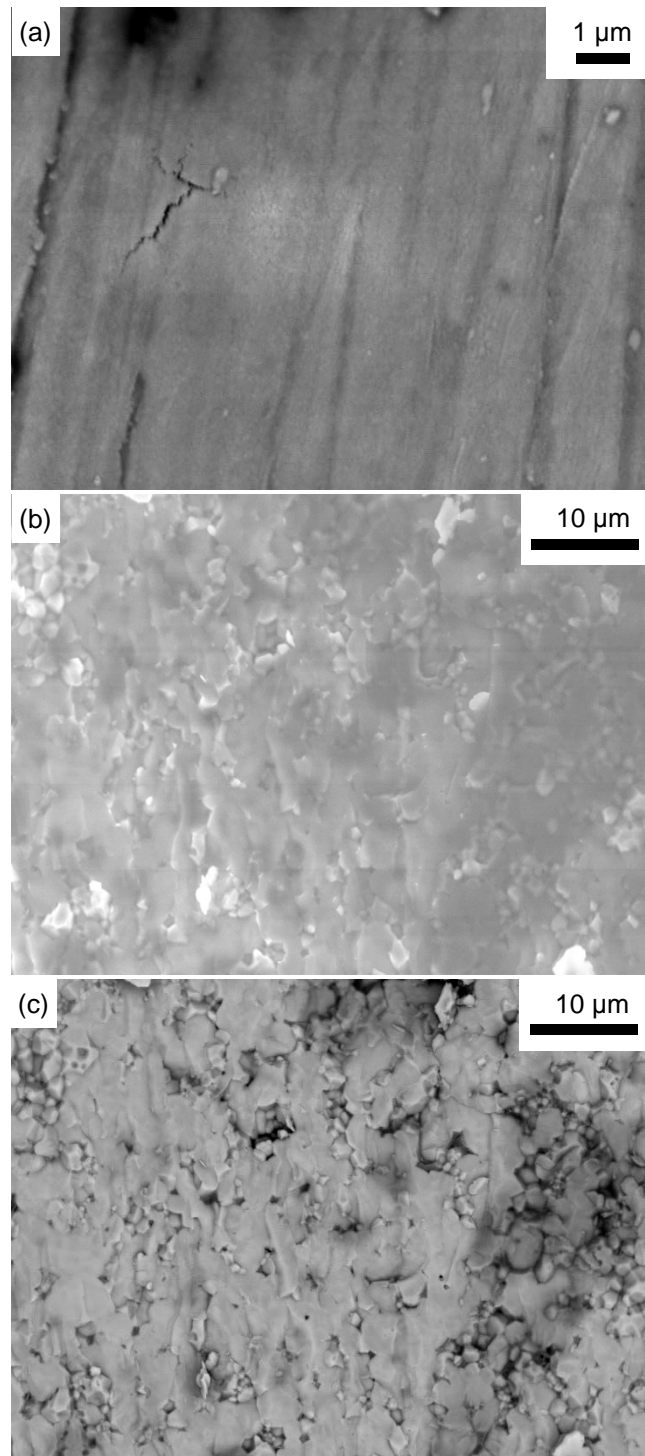


Figure 2. SEM images of a LLZT pellet sintered at 1000°C for 10 min under 25 MPa.

(a) Surface of a pellet prepared by SPS, (b) secondary electron image of fractured cross-

section of a LLZT pellet, (c) reflection electron image of fractured cross-section for the same area as (c).

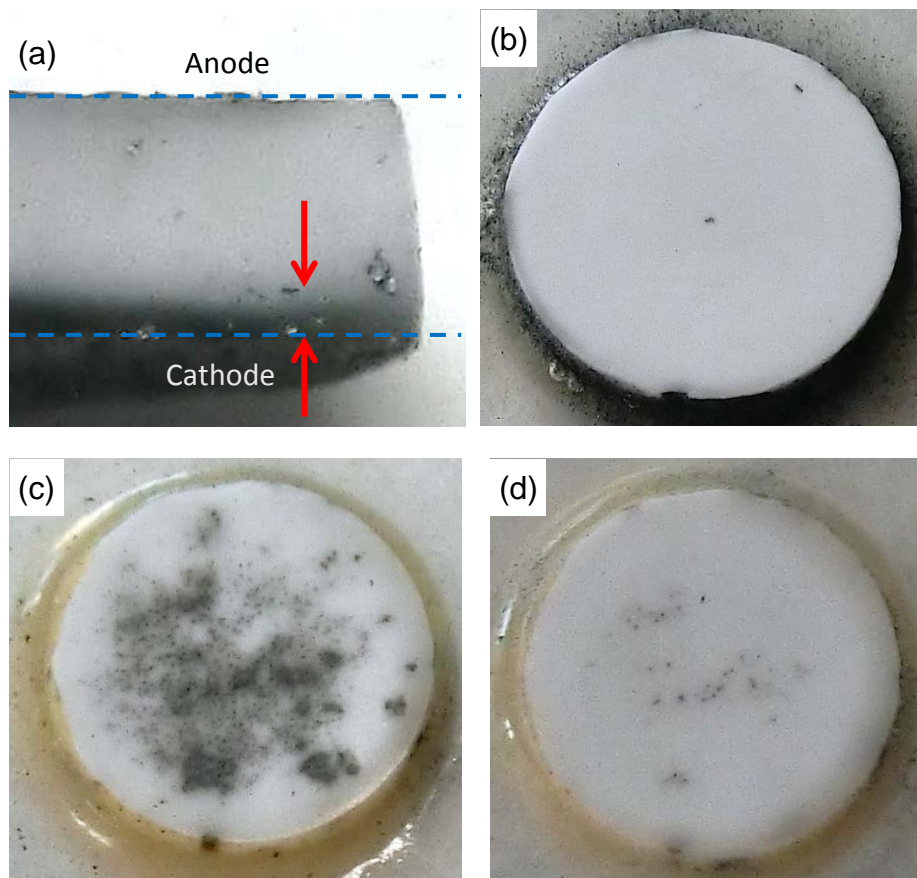


Figure 3. Optical images of an SPS-prepared LLZT pellet sintered at 1000°C for 10 min under 25 MPa. (a) fractured cross-section, (b) surface on the anode after polished by 50 μm, surface on the cathode after polished by (c) 50 μm and (d) 150 μm.

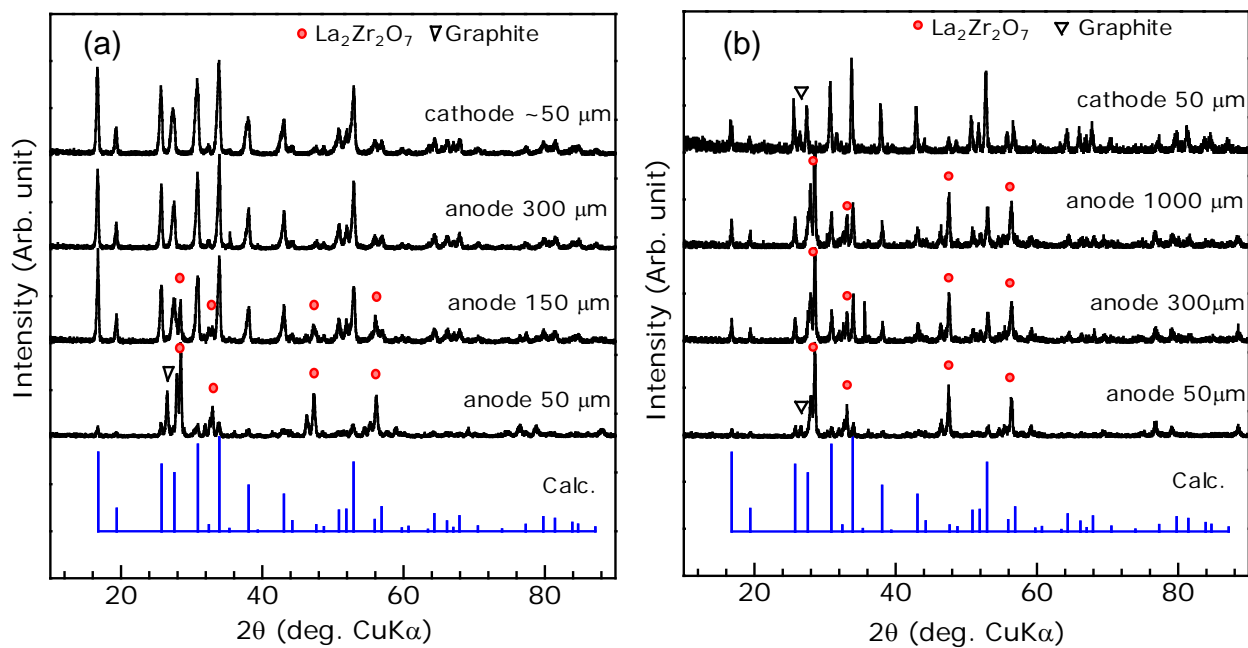


Figure 4. XRD profiles of pellets prepared by SPS using powder with a particle diameter of (a) ca. 1-2 μm and (b) ca. 200 nm. Both pellets were sintered at 1000°C for 10 min under 25 MPa. Surfaces of pellets were polished using emery papers for certain thickness on cathode and anode sides.

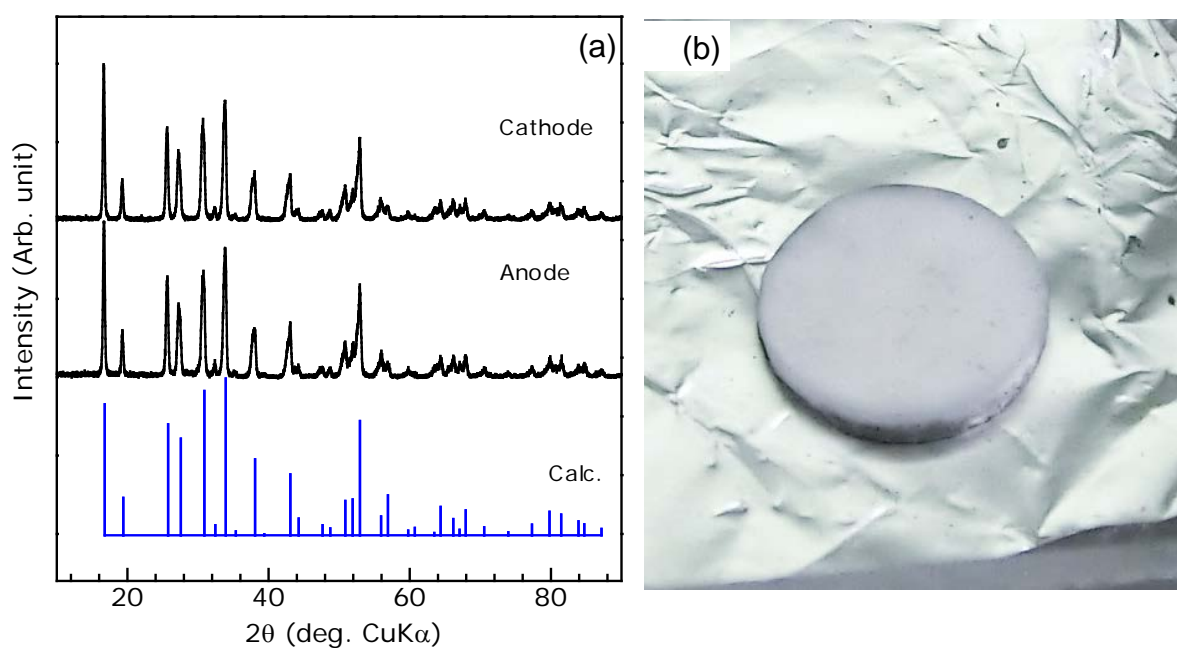


Figure 5 (a) XRD profiles of a LLZT pellet prepared by SPS using LLZT powder without Li_2CO_3 sintered at 1000°C for 10 min under 25 MPa. (b) An optical image of the cathode side of the LLZT pellet prepared without H_2O .

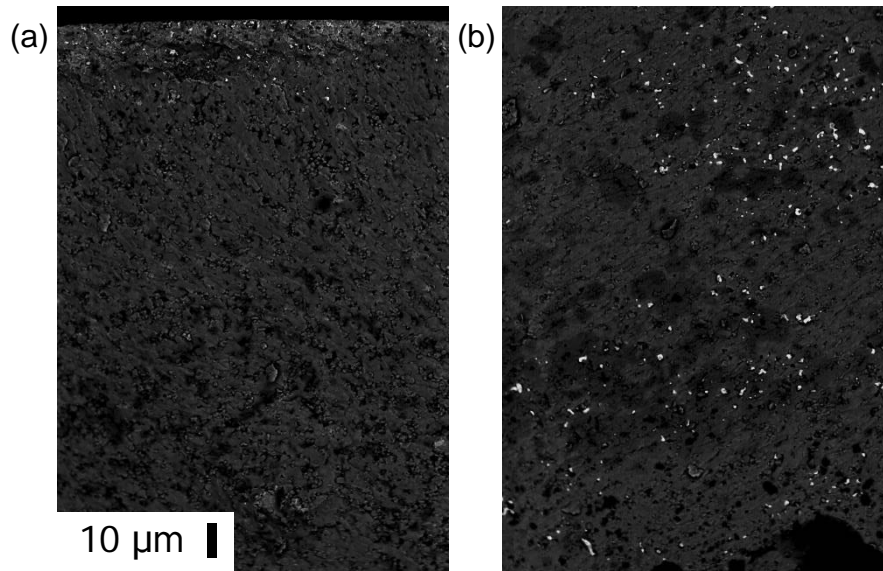


Figure 6. Reflection electron images of (a) anode side and (b) cathode side of fractured cross-section of a LLZT pellet prepared by using Au thin foils instead of graphite sheets.

Note that contrast of images are increased for clarity.

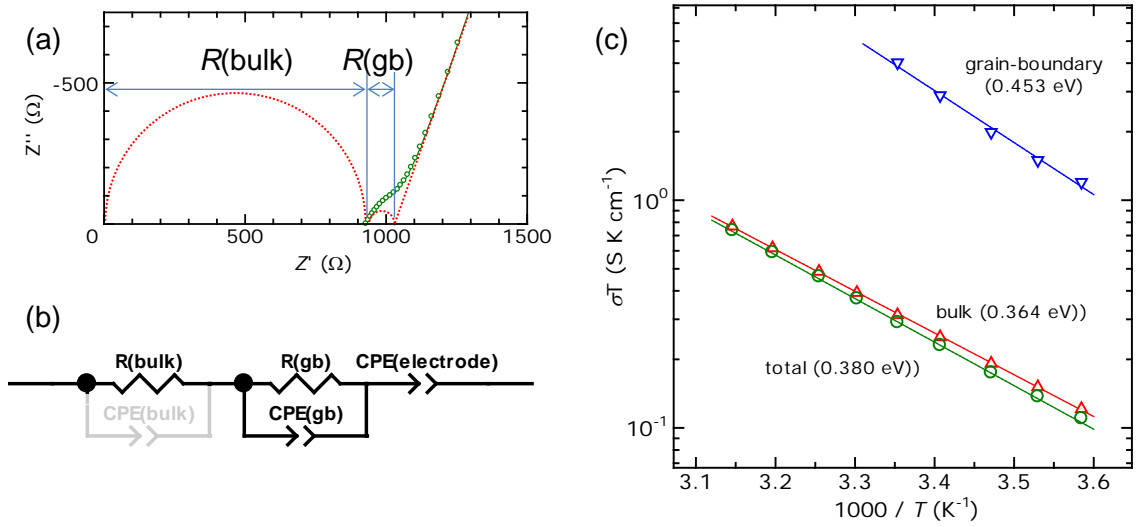


Figure 7 (a) Nyquist plot of a thick LLZT pellet sintered at 1000°C for 10 min under 25 MPa. The surface of pellets was polished to remove impurities. The impedance was recorded at 16°C . (b) An equivalent circuit used for fitting EIS. (c) Temperature dependence of conductivity of bulk, grain-boundary and total.

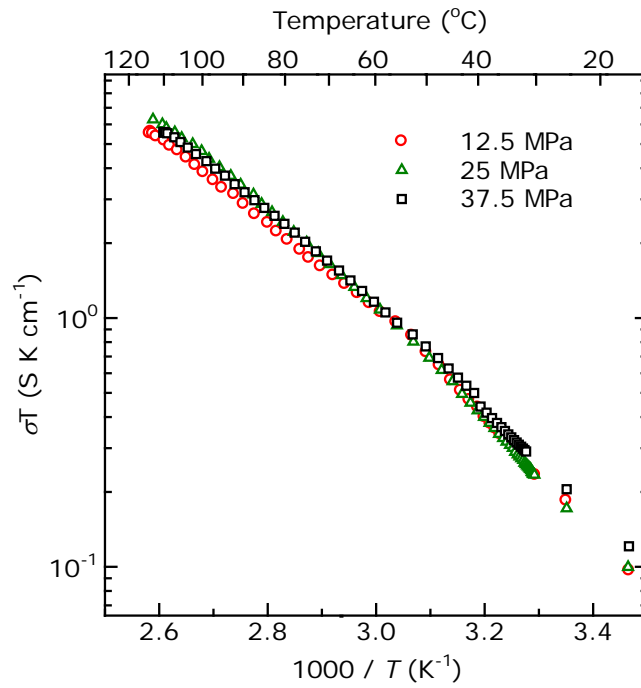


Figure 8 Temperature dependence of conductivity (σ) of LLZT pellets prepared by SPS at 1000°C for 10 min with different uniaxial pressures. The surface of pellets was polished to remove impurities.